Applied Catalysis B: Environmental 217 (2017) 169–180

Contents lists available at ScienceDirect

Applied Catalysis B: Environmental

journal homepage: www.elsevier.com/locate/apcatb

Research Paper

Core-shell g-C_3N_4@ZnO composites as photoanodes with double synergistic effects for enhanced visible-light photoelectrocatalytic activities

Jian Wang[a], Zhuang Yang[a], Xingxing Gao[b], Wenqing Yao[c,*], Weiqin Wei[c], Xianjie Chen[c], Ruilong Zong[c], Yongfa Zhu[c]

[a] School of mining engineering, Engineering Research Center of Green Mining of Metal Mineral Resources, University of Science and Technology Liaoning, Anshan 114051, Liaoning Province, PR China
[b] School of civil engineering, University of Science and Technology Liaoning, Anshan 114051, Liaoning Province, PR China
[c] Department of chemistry, Beijing Key Laboratory for Analytical Methods and Instrumentation, Tsinghua university, Beijing 10084, PR China

A R T I C L E I N F O

Article history:
Received 16 March 2017
Received in revised form 2 May 2017
Accepted 10 May 2017
Available online 11 May 2017

Keywords:
g-C_3N_4
ZnO
Core-shell structure
Synergistic effect
Photoelectrocatalysis

A B S T R A C T

In this work, core-shell g-C_3N_4@ZnO photocatalysts were facilely synthesized via a reflux method applying the industrial grade ZnO nanoparticles and g-C_3N_4 nanosheets as the starting materials. The thickness of the g-C_3N_4 shell was gradually increased with the increasing proportion of g-C_3N_4 and the average thickness of the coating g-C_3N_4 is 1.89 nm and 3.21 nm for a weight ratio of 15% and 20% (g-C_3N_4/ZnO) g-C_3N_4@ZnO composites, respectively. By using g-C_3N_4@ZnO composites as photoanodes for the first time, 15% g-C_3N_4@ZnO photoanode exhibits the best PEC performance for the degradation of phenol under visible light irradiation with an anodic bias of 1.5 V vs. SCE and the rate constant is determined to be 1.216 h^{-1}, which is almost 2.1 times as high as that of 20% g-C_3N_4@ZnO photoanode. The enhancement of the visible light PEC degradation phenol is attributed to the double synergistic effects which combined of special core-shell nanostructures and electro-oxidation assisted photocatalysis. This work not only demonstrates core-shell g-C_3N_4@ZnO composites as a promising photoanode for the utilization of solar conversion, but also meets the requirement for the increasing demand of practical applications

1. Introduction

Solar energy is by far the most abundant source of clean and sustainable energy [1–3]. Semiconductor photocatalysis is highly expected to be a green utilization of the solar energy to decompose various organic compounds for purification of water and air. Until now, a large number of semiconductor materials including metal oxides [4–6], sulfides [7–9], nitrides [10–13], and their mixed solid solutions [14] have been exploited as photocatalysts for photodegradation of organic pollutants and production of H_2. Among semiconductor materials, ZnO is a promising photocatalyst because of its low cost, chemical stability, non-toxicity and high activity in the photocatalytic performance [15–17]. However, some intrinsic properties on ZnO such as its low quantum efficiency, incomplete visible light harvesting and photocorrosion have seriously restricted its commercial applications in the degradation process [18–21]. To efficiently overcome these limitations, many efforts have been made to improve the stability and photocatalytic activity of ZnO-based photocatalysts through metals or nonmetals doping [22–25], deposition of metals [26–28], coupling with visible band gap semiconductor [29–33], and incorporation of carbon allotropes [34–38]. However, the development of efficient ZnO photocatalyst with improved photocatalytic efficiency is still in progress.

More recently, polymeric graphitic carbon nitride (g-C_3N_4) with conjugated π system has received tremendous scientific interest owing to its visible light activity, high chemical stability and especially the suitable band energy position for energy conversion, oxygen reduction and environment purification. However, low quantum efficiency, ultrafast recombination of photoinduced charge carriers and insufficient sunlight absorption currently have limited the practical application of g-C_3N_4. Therefore, many strategies have been developed to improve photocatalytic activity of g-C_3N_4, such as designing nanoporous stuctures [39–41], doping with foreign elements [42–44], texurization [45,46], supermolecular assembly [47,48], coupling wtih graphene [49–51], creating heterojunction [52–54], etc. Among them, construction

* Corresponding author.
E-mail address: yaowq@mail.tsinghua.edu.cn (W. Yao).

http://dx.doi.org/10.1016/j.apcatb.2017.05.034
0926-3373/

heterostructures of coupling g-C_3N_4 with other semiconductors with matching band structures via core-shell structures within highly interactive interfaces is an outstanding approach to achieve efficient separation of photogenerated charges and extend absorption spectrum. For example, S. Kumar et al. reported that N-doped ZnO/g-C_3N_4 core-shell nanoplates have been prepared via an ultrasonic dispersion method [21]. The improved performance demonstrates the importance of valuating new core-shell composites photocatalysts with shell material g-C_3N_4. Pan et al. has prepared the g-C_3N_4/$BiPO_4$ and g-C_3N_4/$BiWO_6$ core-shell structures with greatly enhancing photocatalytic activities [55,56]. Chen et al. has synthesized ZnO@mpg-C_3N_4 photocatalysts with core-shell structure via an ultrasonic dispersion method [17]. R. C. Pawar et al. integrated ZnO with g-C_3N_4 nanostructures via successful core-shell formation using single step simple sintering process [57]. This enhanced photocatalytic performance of core-shell composites was aroused from effective interfacial charge separation and transportation. Although, g-C_3N_4@ZnO core-shell heterostructures have been reported for photocatalytic applications, to the best of our knowledge, little attention has been paid to the detailed relationship between g-C_3N_4 shell thickness and photoelectrocatalytic properties of g-C_3N_4@ZnO composite photocatalysts.

In order to greatly improve the quantum efficiency of photocatalytic process, the photoelectrocatalytic (PEC) process, the combination of photocatalysis (PC) and electrolysis (EC) has been represented to be a more promising strategy and more efficient than individuals [58]. In this study, core-shell g-C_3N_4@ZnO photocatalysts immobilized onto a conductive ITO substrate was used as the photoanodes for the first time and an external anodic potential bias was applied to inhibit the recombination of holes and electrons, thus greatly improving the efficiency of the degradation of phenol. In addition, coupling industrial grade ZnO nanoparticles with g-C_3N_4 via core-shell structures meet the requirements for practical applications.

Herein, our strategy uses the industrial grade ZnO nanoparticles and exfoliated g-C_3N_4 nanosheets as the starting materials to prepare a series of g-C_3N_4@ZnO composites by a simple reflux method at a low temperature. The influence of different loading amount g-C_3N_4 on the thickness of the g-C_3N_4 shell which is closely connected with the PC, EC and PEC activity, has been systematically examined, as it is remain unaddressed in most of the papers on g-C_3N_4@ZnO core-shell structures. Remarkably, g-C_3N_4@ZnO composites were used as the photoanodes for the first time and they showed superior PEC activities in decomposing phenol with an anodic bias of 1.5 V vs. SCE under visible light irradiation with respect to pure g-C_3N_4 photoanode. Base on the double synergistic effects of core-shell structure and electro-oxidation assisted photocatalysis, the possible mechanisms of the visible-light enhancement of PEC activity was discussed.

2. Experimental

2.1. Preparation of g-C_3N_4@ZnO core-shell photocatalysts

ZnO (particle diameter 30–50 nm) was purchased from Nanjing Haitai Nanometer Materials Corp, P. R. China; Melamine ($C_3H_6N_6$) was obtained from Tianjin Fuchen Chemical Reagents factory, P. R. China. All chemicals used in this research were reagent grade and used without further purification. The g-C_3N_4 was prepared by heating melamine to 550 °C with a ramping rate of 2 °C/min for 4 h according to the literature [59]. The product was collected and ground into powder in an agate mortar for further use. The g-C_3N_4 nanosheets were obtained by concentrated H_2SO_4 exfoliation method, which was reported in our previous literature [60]. Fig.S1 shows TEM images of bulk g-C_3N_4 and concentrated H_2SO_4 exfoliation of g-C_3N_4 nanosheets.

The resultant pale yellow g-C_3N_4 nanosheets were collected for further use. The g-C_3N_4@ZnO core-shell photocatalysts were synthesized through a facile reflux method. The procedure of preparation is as follows: firstly, the different amount g-C_3N_4 nanosheets (0.01, 0.05, 0.10, 0.15, 0.20 g) were added into 100 mL methanol then the beaker was placed in an ultrasonic bath for 30 min to completely disperse the nanosheets. Then 1 g ZnO was introduced into the above solution in sequence, which was continually stirred for 30 min. After being stirred vigorously, the solution was transferred into a 250 mL round-bottom flask which was magnetically stirred and refluxed for 14 h at 65 °C, and then allowed to cool naturally to room temperature. After evaporation of the methanol, the opaque powder was obtained. Different mass ratios of g-C_3N_4@ZnO photocatalysts were obtained under vacuum at 80 °C for 4 h.

2.2. Preparation of the g-C_3N_4 and g-C_3N_4@ZnO film photoelectrode

The indium-tin oxide (ITO) glass (thickness 1.1 mm and a sheet resistance 15 Ω/) was used as substrate, which was purchased from China Southern Class Co., Ltd. The ITO glass were immersed in a mixture solution of NaOH (1 mol L^{-1}) and H_2O_2 (30%), and then washed with acetone, alcohol and deionized water via ultrasonication, followed by drying the samples in the flow of N_2 atmosphere. The immobilized g-C_3N_4 and g-C_3N_4@ZnO photoanodes were deposited on ITO glass substrates through a dip-coating process according to our previous work [61]. In a typical process, 100 mg of the g-C_3N_4@ZnO composites and g-C_3N_4 were dispersed in 100 mL of water under sonication for 6 h. The ITO glass was immersed vertically into the g-C_3N_4@ZnO composites and g-C_3N_4 aqueous dispersion, and the dip coating parameter for g-C_3N_4@ZnO composites and g-C_3N_4 were taken as follows: lifted height: 40 mm, elevated rate: 30 μm/s, resident time: 30 s, immerse time: 60 s. The dip-coating process was repeated 5 times to obtain a multilayer film (g-C_3N_4@ZnO and g-C_3N_4). Finally, the prepared films were treated at 80 °C for 30 min under N_2 flow after each dipping and obtained working photoanodes. FESEM images of 15% g-C_3N_4@ZnO photoanode are shown in Fig.S2.

2.3. Characterization of g-C_3N_4 and g-C_3N_4@ZnO photocatalysts

The as-synthesized samples were examined by X-ray diffractometry (XRD) measurement on a Bruker D8 Advance X-ray diffractometer equipped with graphite monochromatized CuKα (λ = 1.5406 Å) at 40 kV and 40 mA. The transmission electron microscopy (TEM) and the field emission gun scanning electron microscope (FESEM) were recorded on a JEM 2010F and Hitachi SU-8010, respectively. The diffuse reflectance absorption spectra (DRS) of the samples were recorded in the range of 200–900 nm on a UV–vis spectrophotometer (Hitachi UV-3010) equipped with integrated sphere attachment, and $BaSO_4$ was used as a reference. The Brunauer-Emmett-Teller (BET) specific surface area and the pore distribution of the samples were evaluated by N_2 adsorption/desorption using Beishide Instrument-ST, 3H-2000PS2. Fourier transform infrared (FT-IR) spectra were carried out using Bruker V70 spectrometer with a resolution of 1 cm^{-1}. Photoluminescence (PL) spectra of the samples were recorded on a JASCO FP-6500 at room temperature with an excitation light of 375 nm.

2.4. Photoelectrochemical measurements and degradation of phenol with different process

Electrochemical and photoelectrochemical measurements which were recorded with an electrochemical system (CHI-660D,

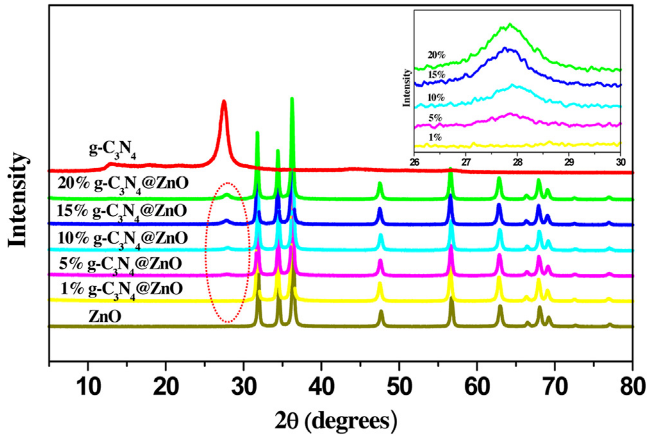

Fig. 1. XRD patterns of ZnO, g-C_3N_4 and g-C_3N_4@ZnO composites, the inset shows the magnified XRD patterns g-C_3N_4@ZnO composites taken from the red elliptical area. (For interpretation of the references to colour in this figure legend, the reader is referred to the web version of this article.)

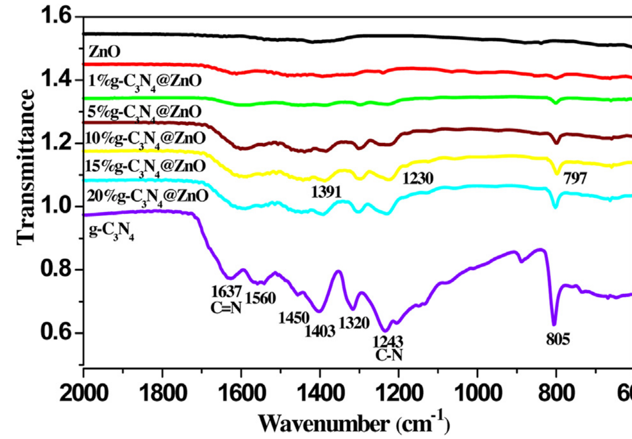

Fig. 2. FT-IR spectra of ZnO, g-C_3N_4 and g-C_3N_4@ZnO composites.

China) were performed in a three-electrode quarts cells with 0.1 M Na_2SO_4 electrolyte solution. Platinum wire (70 mm in length with a 0.4 mm diameter) was used as counter and saturated calomel electrode (SCE) used as reference electrodes, respectively, and g-C_3N_4@ZnO photoanodes on ITO served as the working electrode (active area of 6 cm^2). The photoanodes were irradiated with visible light provided by 500 W Xe lamp (Institute for Electric Light Sources, Beijing) with 420 nm optical filters and the average visible light intensity was 23.6 mW cm^{-2}. UV light was provided by a 300 W mercury lamp (365 nm) and the average light intensity was 1.3 mW cm^{-2}.

The PC, EC and PEC degradation of phenol was performed in a three-electrode system, which connected with a counter electrode (Pt wire with 70 mm in length and 0.4 mm diameter), saturated calomel electrode (SCE) using as reference electrodes, and g-C_3N_4@ZnO films electrodes on ITO serving as the photoanodes (active area of 6 cm^2). The reactive system containing the mixture solution 100 mL (0.1 M Na_2SO_4 electrolyte solution and 5 ppm phenol) was placed 5 cm away from a 500 W Xe lamp with 420 nm optical filters. The applying biased voltage was performed on an electrochemical system (CHI-660D, China). Before PC, EC and PEC degradation of phenol, the dispersed solution was magnetically stirred in the dark for 1 h to ensure absorption-desorption equilibrium. At a defined time intervals, 3 mL suspension were collected and centrifuged to remove the samples. Subsequently, the phenol and intermediate degradation products solution were injected to HPLC (high performance liquid chromatography) system. The phenol concentration and its degradation intermediate products were detected an HPLC system equipped with an UV–vis K2501 detector, a Venusil XBP-C_{18} column (Agela Technologies Inc.) and an auto-sampler (20 vial capacity with 6 line degasser channels).

3. Results and discussion

3.1. Formation of core-shell structure g-C_3N_4@ZnO composites

The XRD patterns of ZnO, g-C_3N_4 and g-C_3N_4@ZnO composites with the different loading amount of g-C_3N_4 were shown in Fig. 1. The pure g-C_3N_4 of two pronounced peaks at 27.48°and 12.97°which correspond to interlayer stacking of aromatic segments and tri-striazine units of g-C_3N_4 phase assigned to (100) and (002) planes, respectively [62]. The diffraction peaks of pristine ZnO can be exactly indexed as the hexagonal wurtzite structure (JCPDS 89–1397). There was no ZnO crystalline change with containing different amounts of g-C_3N_4. Additionally, the XRD patterns in the region of 2θ (26–30°) are given inset of Fig. 1 for better comparison. The diffraction peaks of crystalline g-C_3N_4 cannot be observed in the g-C_3N_4@ZnO photocatalyst with low loading amount of g-C_3N_4 (1%). With the increased loading amount of g-C_3N_4 to 5%, a weak peak at 27.87° appears. When the loading amount of g-C_3N_4 further increasing, the intensity of the (002) diffraction peak of g-C_3N_4 becomes gradually enhanced. Meanwhile, the peaks of ZnO planes of the g-C_3N_4@ZnO composites were slightly shifted to a lower angle than those for pure ZnO, but the diffraction peak (002) g-C_3N_4 planes in the composites slightly were shifted to higher angles than pure g-C_3N_4. This effect indicates a strong interaction between ZnO and g-C_3N_4 in the g-C_3N_4@ZnO composites, suggesting that g-C_3N_4 nanosheets which cannot manipulate the lattice structure of ZnO have successfully attached to the surface of ZnO nanoparticles. Furthermore, no other impurity crystal phases was seen, indicating the g-C_3N_4@ZnO is a two-phase composition.

Fig. 2 shows the FT-IR spectra of g-C_3N_4, ZnO and various g-C_3N_4@ZnO composites. Based on previous reports of g-C_3N_4, the peaks at 1637 cm^{-1} and 1243 cm^{-1} were assigned to the C═N and C—N stretching vibration modes, respectively [63]. Moreover, the peak at 805 cm^{-1} is assigned to the out of plane breathing vibration characteristic of s-triazine ring system [64]. In addition, the peaks at 1403, 1450, 1560, 1637 cm^{-1} are likely due to heptazine-derived repeating units [65]. The FT-IR spectra of various g-C_3N_4@ZnO composites have presented the main characteristic peaks of g-C_3N_4 and these main characteristic peaks (805, 1243 and 1403 cm^{-1}) of g-C_3N_4 shifted to a lower wave number compared with pure g-C_3N_4, which is due to the weakened bond strength of C—N and C═N. Moreover, with the increase of the loading amount of g-C_3N_4, the intensities of main characteristic peak of g-C_3N_4 in the g-C_3N_4@ZnO composites increase. The mention above indicates that there was a covalent bond between g-C_3N_4 and ZnO rather than a physical mixing, suggesting that extended conjugated systems were generated in the g-C_3N_4@ZnO composites. This chemical bond was of great significance for the charge transfer and the stability of such core-shell g-C_3N_4@ZnO structure.

TEM was applied to testify the formation of core-shell structure and to estimate g-C_3N_4 shell thickness. TEM/HRTEM analysis of pristine ZnO and g-C_3N_4@ZnO composites with the different loading amount of g-C_3N_4 were shown in Fig. 3. It can be seen from Fig. 3a that pristine ZnO is composed of a large scale of nanoparticles with a diameter range from 30 to 50 nm. The HRTEM images of 1%, 5% and 10% g-C_3N_4@ZnO composites are shown in Fig. 3b–d, respectively. As the loading amount of g-C_3N_4 increased from 1 to 10%, the edge of ZnO nanoparticles becomes rough as compared with pure ZnO and the core-shell structure of g-C_3N_4@ZnO can hardly be observed in HRTEM images. As can be seen from Fig. 3b–d, the d-

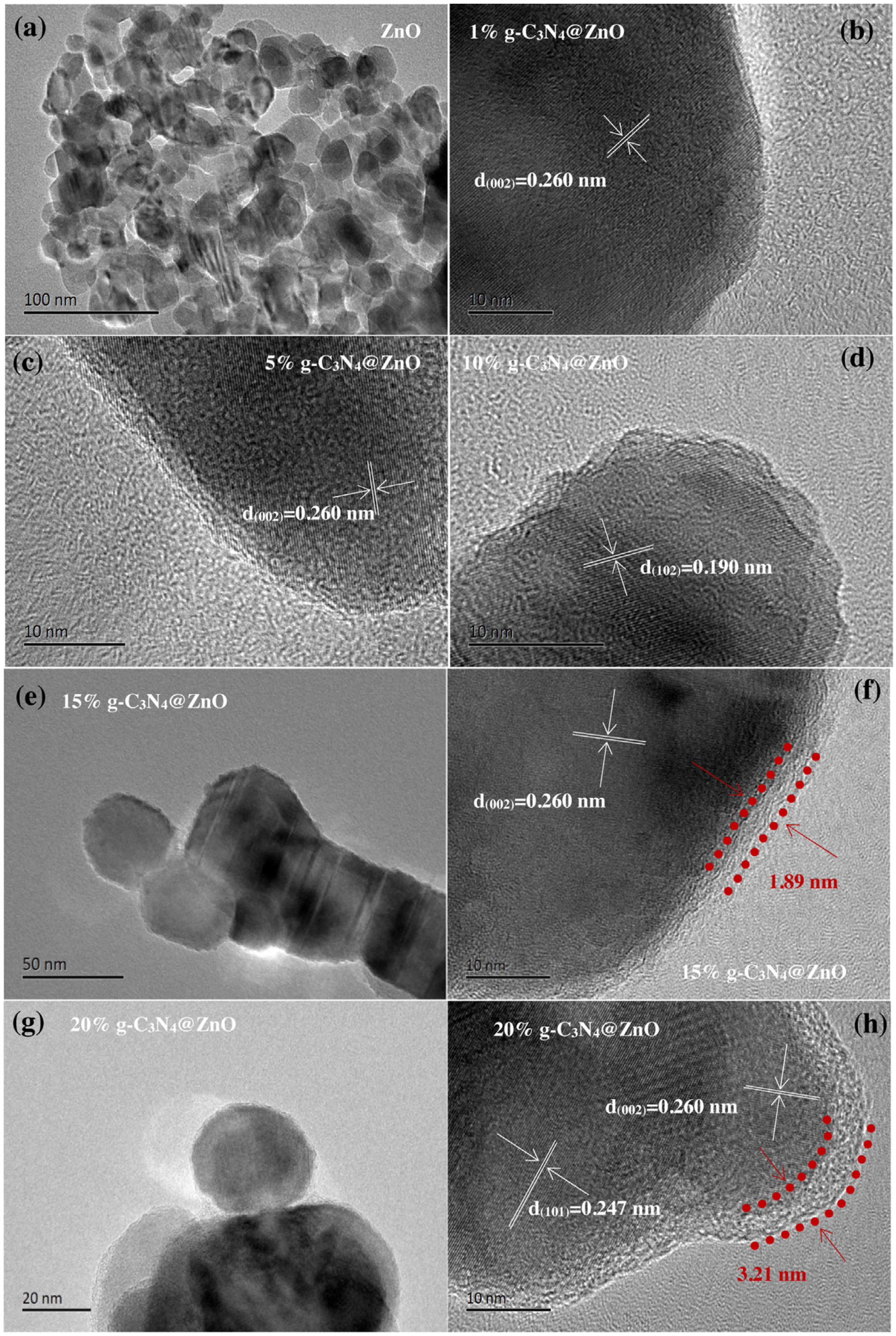

Fig. 3. TEM and HRTEM images of ZnO and g-C_3N_4@ZnO composites. (a) TEM image of ZnO nanoparticles. (b to d) HRTEM images of 1%-10% g-C_3N_4@ZnO composites. (e and f) TEM and HRTEM images of 15% g-C_3N_4@ZnO composites. (g and h) TEM and HRTEM images of 20% g-C_3N_4@ZnO composites.

spacing of ZnO is 0.260, 0.260 and 0.190 nm, corresponding to (002), (002) and (102) interlayer spacing respectively, indicating there is no change in the lattice structure of ZnO after loading g-C_3N_4. Fig. 3e and f show HRTEM images of g-C_3N_4@ZnO composites with loading amount of 15% g-C_3N_4. It shows clearly obvious interface between g-C_3N_4 and ZnO nanoparticles and very thin amorphous layer could be observed, suggesting ZnO nanoparticles are coated with g-C_3N_4 layers. The average thickness of the coating g-C_3N_4 shell could be measured about 1.89 nm on the surface of ZnO nanoparticles. The outer boundary of as-synthesized samples is completely distinct from the ZnO core and the orderly inter-planar spacing is 0.260 nm, corresponding to (002) plane. For 20% g-C_3N_4@ZnO composites (Fig. 3g and h), the g-C_3N_4 shell is thicker than 15% g-C_3N_4@ZnO composites and it is increased to 3.21 nm. The lattice structure is highly orderly with spacing of 0.260 and 0.247 nm, corresponding to the (002) and (101) planes of ZnO, respectively. Fig.S3 illustrates the detailed formation process of core-shell structure g-C_3N_4@ZnO composites. Base on the above results, the loading amount of g-C_3N_4 plays a most important role in forming such core-shell structure composites. Therefore, it is concluded that as-

synthesized samples are not a physical mixture of two components and only the loading amount of g-C_3N_4 is more than 15% for the formation of the core-shell well-construction. Moreover, g-C_3N_4 shell increases with an increasing of the amount of g-C_3N_4, indicating that it may be regulated by precise control the amount of g-C_3N_4. Furthermore, the core-shell structure is achieved, which could lead to the formation of intimate interactions between ZnO core and g-C_3N_4 shell, thus facilitating the migration of the photogenerated charge carriers and improving photocatalytic efficiency.

3.2. Photoelectrocatalytic activity of core-shell structure g-C_3N_4@ZnO photocatalyst

The UV–vis DRS spectra of ZnO, g-C_3N_4 and different mass ratios of g-C_3N_4@ZnO composites are shown in Fig. 4. The band gaps of (E_g) samples were calculated from the onsets of the absorption edges using formula $\lambda_g = 1239/E_g$, where λ_g is the band-gap wavelength [66]. As shown in Fig. 4, pure ZnO has a fundamental absorption edge at 396 nm, corresponding to a band gap of 3.13 eV, which signifies its photocatalytic activity under UV irradiation and meanwhile the absorption edge of g-C_3N_4 appeared at 460 nm, corresponding to band gap of 2.69 eV. It is notable that compared with pure ZnO, the absorption edge of g-C_3N_4@ZnO composites significantly extended up to the visible-light region and showed an evident red shift gradually with an increasing loading amount of g-C_3N_4, suggesting that the band gaps of these composites are reduced. The g-C_3N_4@ZnO composites exhibit a strong visible-light absorption, indicating that strong interaction through the tight chemically bonded interfaces between ZnO core and g-C_3N_4 shell extends visible light response which leads to the generation of more photogenetated electrons and holes and thus enhanced photocatalytic activity.

The transient photocurrent response of ZnO, g-C_3N_4 and g-C_3N_4@ZnO composites electrodes were recorded to investigate the interfacial electronic interaction between g-C_3N_4 shell and ZnO core (Fig. 5a and b). Fig. 5a shows the current-voltage curves for the film electrodes with several on-off cycles of intermittent visible-light irradiation ($\lambda > 420$ nm) in 0.1 M Na_2SO_4 aqueous solution. With an increasing of the loading amount of g-C_3N_4, the photocurrent response of g-C_3N_4@ZnO composites increases, reaching a maximum photocurrent at loading amount of 15% g-C_3N_4, and then followed by a decreasing trend with a further increase of g-C_3N_4 loading up to 20%, which may be associated with the shell thickness of g-C_3N_4. The excessive shell thickness of g-C_3N_4 may impede the separation and migration of photogenerated carriers in the g-C_3N_4@ZnO composites under visible light irradiation. The g-C_3N_4@ZnO composites with loading amount of 15% g-C_3N_4 shows the strongest photocurrent response (*ca.* 12.2 μA), which is nearly 2 times and 10 times higher than that of 20% g-C_3N_4@ZnO (*ca.* 6.2 μA) and bulk g-C_3N_4 (*ca.*1.2 μA), due to the synergistic effect between ZnO core and g-C_3N_4 shell. Moreover, after four on-off cycles, the photocurrent of 15% g-C_3N_4@ZnO composites showed no obvious decay, indicating that the separation and migration of photogenerated carriers has a relatively steady photoelectrochemical performance. The results revealed that 15% g-C_3N_4@ZnO composites with the appropriate g-C_3N_4 shell thickness of 1.9 nm may achieve more effective charge separation and photocatalytic activity than that of other g-C_3N_4@ZnO composites and pure g-C_3N_4. However, g-C_3N_4@ZnO composites do not show a positive effect in the enhancement of the photocurrent compared to ZnO under UV light irradiation. It can be seen from Fig. 6b that the photocurrent under UV light irradiation ($\lambda > 365$ nm) was in order of *I*(ZnO) > *I*(1% g-C_3N_4@ZnO) > *I*(5% g-C_3N_4@ZnO) > *I*(10% g-C_3N_4@ZnO) > *I*(15% g-C_3N_4@ZnO) > *I*(20% g-C_3N_4@ZnO). In addition, the photocurrent responses of g-C_3N_4@ZnO composites dramatically decreased to a great extent when loading amount of g-C_3N_4 was up to 10%, which suggested that the separation efficiency of photogenerated carriers of g-C_3N_4@ZnO composites greatly deteriorated. The decreased photocurrent above optimal loading amount of g-C_3N_4 may be due to the fact that such g-C_3N_4 shell may shield UV light of ZnO core. The electrocatalytic activity of ZnO, g-C_3N_4 and 15% g-C_3N_4@ZnO composites for the oxidation of phenol under dark and under visible light illumination was investigated in Fig. 5c by recording CVs in an aqueous solution of Na_2SO_4 (0.1 M), with 5 ppm phenol, at a sweep rate of 50 mVs^{-1} in the potential window of 0.4–1.5 V. It is interesting to notice that ZnO electrode of oxidation current is, in both cases under dark and under visible light illumination, very similar in shape and size, indicating that ZnO almost have no response to visible light irradiation. The anodic peak current of 15% g-C_3N_4@ZnO electrode is significantly higher than that of ZnO electrode, suggesting that 15% g-C_3N_4@ZnO electrode involving faster electron transfer, shows a good electrocatalytic effect towards the phenol oxidation. In comparison with the 15% g-C_3N_4@ZnO electrode under the dark condition, 15% g-C_3N_4@ZnO electrode under visible light irradiation showed two obvious changes: first, the peaks of redox potential lead to a negative potentials shift; second, an increase on the oxidation peak current was observed, indicating that the strong interaction between ZnO core and g-C_3N_4 shell improved the interfacial electron transfer and induced the significant enhancement of synthetic effect towards the phenol oxidation in the presence of visible light. However, the g-C_3N_4 electrode shows a lower oxidation current and yields a trace of current over the same applied potential range with or without visible light irradiation, indicating a depressed interfacial electron transfer at g-C_3N_4 electrode. To investigate the effect of g-C_3N_4 shell modification, the PL spectra were used to reveal the transfer and recombination process of photogenerated e-h pairs in the core-shell g-C_3N_4@ZnO composites system. Fig. 5d displays the PL spectra of pure g-C_3N_4, 15% and 20% g-C_3N_4@ZnO under excitation wavelength of 365 nm. It can be seen that the PL spectra of pure g-C_3N_4 shows a strong peak at around 460 nm, which suggests high recombination rate of the photoexcited electron-hole of g-C_3N_4. The g-C_3N_4@ZnO composites show the peak at 460 nm and a little sharp peak around 385 nm, which was attributed to presence of surface oxygen vacancies and zinc defects [32]. After the g-C_3N_4 shell is introduced into the modification of ZnO, the intensity of PL around at 460 nm decreases remarkably and 15% g-C_3N_4@ZnO composites is the lowest intensity of all, suggesting that the suitable g-C_3N_4 shell thickness in the g-C_3N_4@ZnO composites can effectively separate charge transfer and suppress the recombination of electron-hole. It can be inferred that the excess g-C_3N_4 shell thickness can be a recombination center of photogenerated electrons and holes, thus inducing more recombination. The PL results are consistent with the results of visible-light photocurrent response.

The degradation of phenol solution in different process such as PC, EC, and PEC activity was conducted on the as-synthesized g-C_3N_4@ZnO composites and g-C_3N_4 under visible light and UV light illumination with an anodic bias of 1.5 V vs. SCE. According to previous study, phenol molecule is stable and self-degradation effect of phenol solution is almost neglected under light irradiation [58]. From Fig.S4, phenol solution maintains constant in dark, suggesting adsorption hardly occurs on the g-C_3N_4@ZnO photoanodes. The pseudo-first-order kinetics model was employed to fit the PC, EC and PEC degradation process and the kinetic constant k is equal to the corresponding slope of the fitting line [67]. It is noteworthy that PC, EC and PEC degradation phenol under visible light irradiation are rather different; the kinetic constant k value of as-syntesized samples follows the same order, which was similar to trend to the visible-light photocurrent. As can be seen from Fig. 6a, by comparing with pristine g-C_3N_4, all of the g-C_3N_4@ZnO composites exhibited significantly enhanced higher photocatalytic activity under visible light irradiation ($\lambda > 420$ nm). The photocatalytic per-

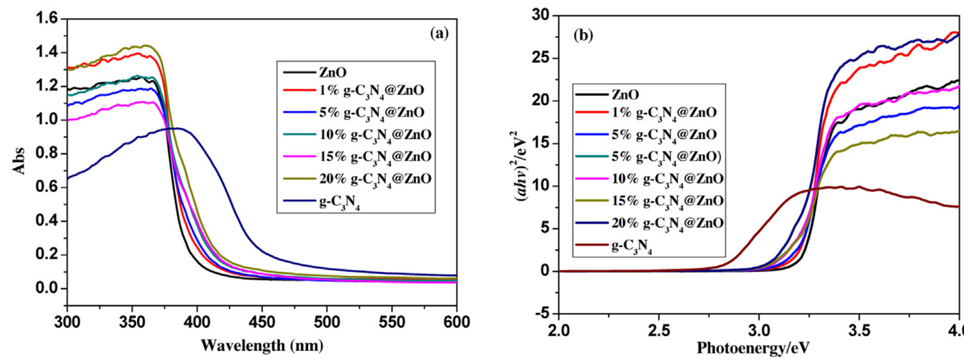

Fig. 4. (a) UV–vis diffuse reflection spectra of ZnO, g-C_3N_4 and g-C_3N_4@ZnO composites. (b) The plots $(ahv)^2$ versus energy (hv) for the band gap energies by using Kubelka-Munk function.

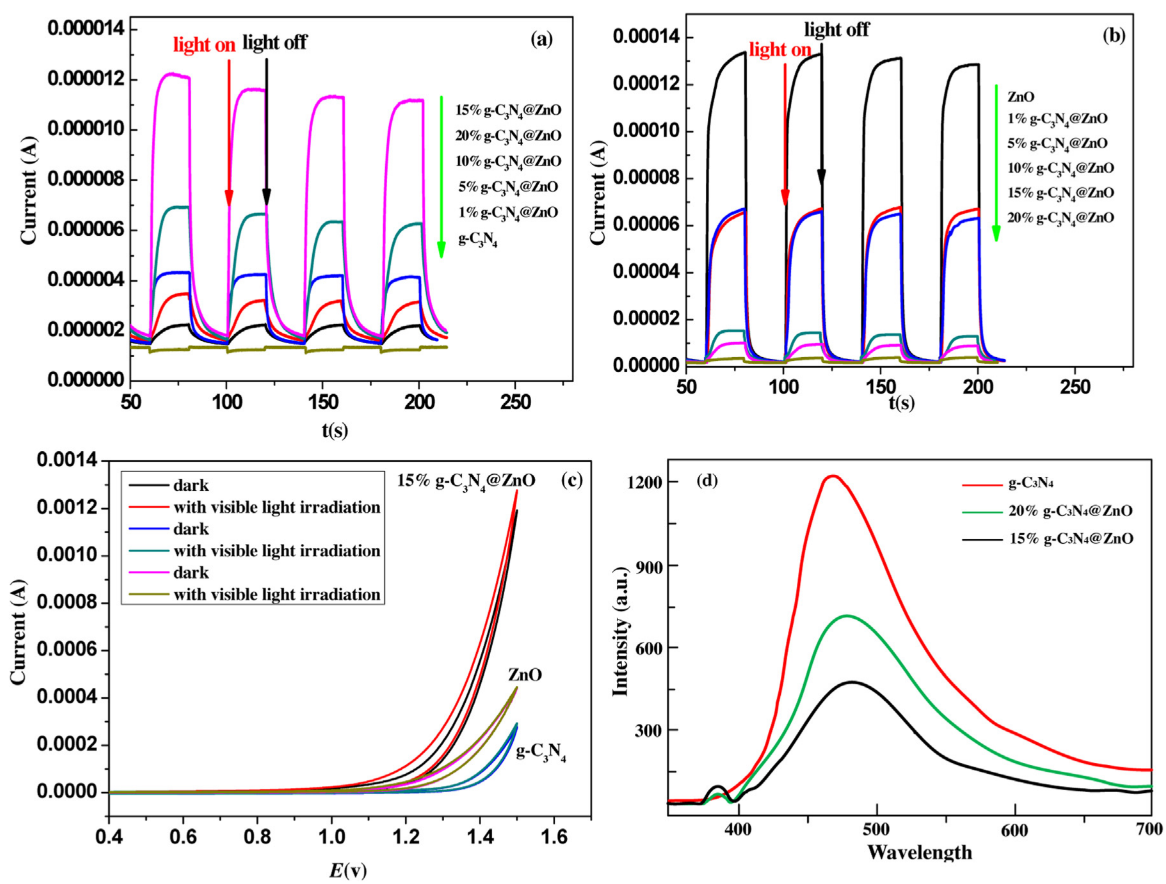

Fig. 5. The photocurrent of the g-C_3N_4@ZnO electrodes (a) under visible light irradiation; (b) UV light irradiation; (c) CVs of 15% g-C_3N_4@ZnO, ZnO and g-C_3N_4 electrodes with and without visible-light irradiation; (d) Photoluminescence spectra (excited at 365 nm) of prepared samples.

formance of g-C_3N_4@ZnO increases gradually with an increasing of the loading amount of g-C_3N_4 and 15% g-C_3N_4@ZnO composites shows dramatically enhanced photocatalytic performance. The corresponding k value is $0.396\,h^{-1}$, which is about 5.0 times that of g-C_3N_4 ($0.079\,h^{-1}$), indicating that the core-shell structure enhanced photocatalytic performance by the effective separation of charge carries in the interface of ZnO core and g-C_3N_4 shell. This result clearly illustrates the importance of the amount of g-C_3N_4 in the g-C_3N_4@ZnO composites to the photocatalytic activity and there exists a significant synergistic effect between g-C_3N_4 shell and ZnO core for photocatalytic degradation of phenol under visible light irradiation. This synergistic effect between the improved absorption of visible light by g-C_3N_4 shell and polarization field provided by the ZnO core facilitates photogenerated charge separation and interfacial transfer. However, with the loading amount of g-C_3N_4 further increasing to 20%, the apparent rate constant k of 20% g-C_3N_4@ZnO decreased to $0.215\,h^{-1}$ though it remains higher than that of g-C_3N_4. This implies that loading amount of g-C_3N_4 had a great influence on the photocatalytic activity of the as-synthesized photocatalysts. Too much loading amount g-C_3N_4 results in an increasing g-C_3N_4 shell thickness, causing a longer transportation pathways of the photoinduced electrons in the g-C_3N_4 shell, thus decreasing efficiency of photogenerated charge separation and transfer. Therefore, an appropriate amount ratio of g-C_3N_4 and ZnO are important to core-shell structure g-C_3N_4@ZnO composites. In other words, there is a suitable g-C_3N_4 shell thickness in the g-C_3N_4@ZnO composites, and the optimal g-C_3N_4 shell thickness is 1.91 nm in the present study. The synergistic effect in

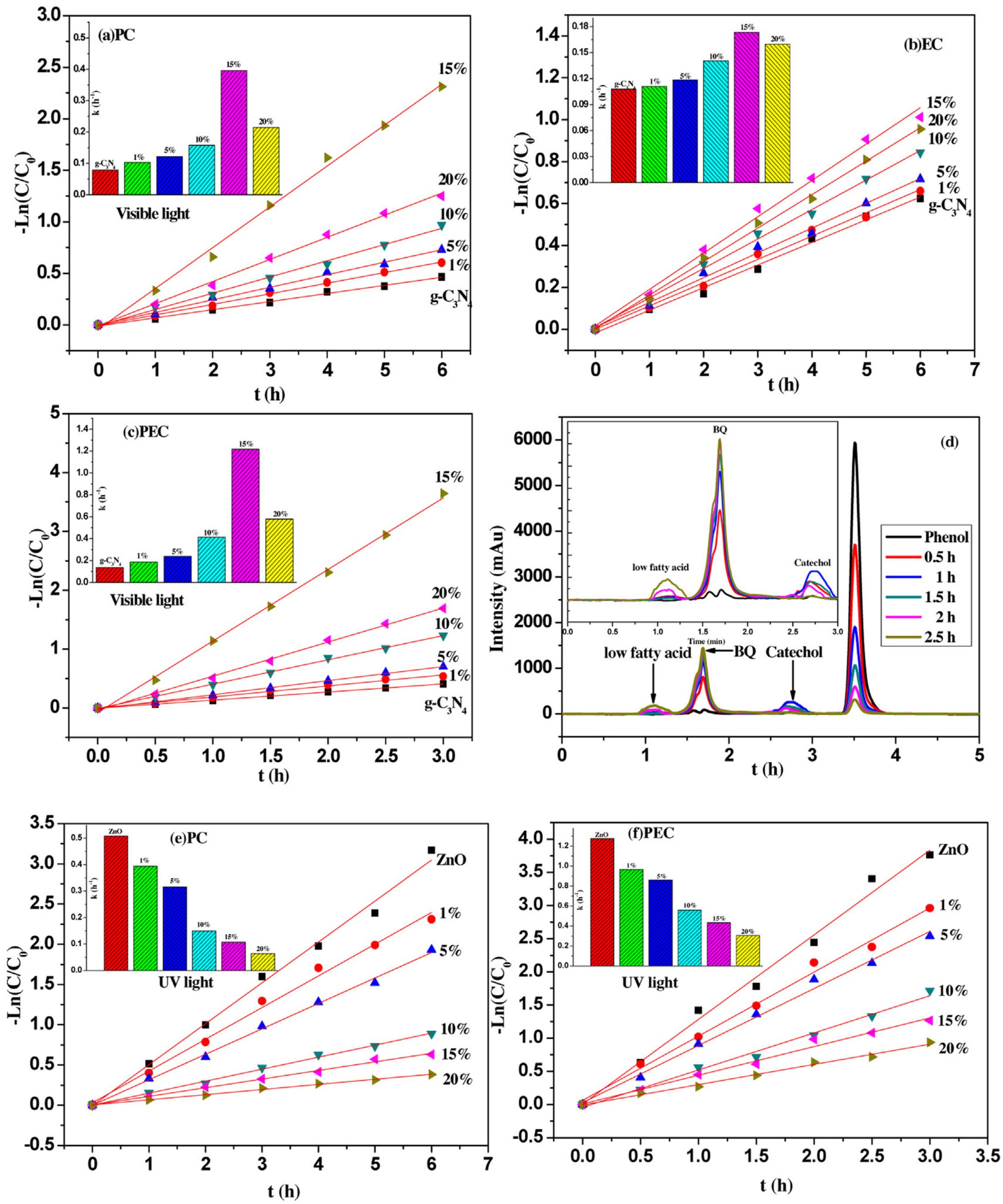

Fig. 6. (a) PC degradation rate of phenol using g-C_3N_4 and g-C_3N_4@ZnO photoanodes under visible light irradiation ($\lambda > 420$ nm). (b) EC degradation rate of phenol over g-C_3N_4 and g-C_3N_4@ZnO electrodes at an applied potential of 1.5 V. (c) PEC degradation rate of phenol over g-C_3N_4 and g-C_3N_4@ZnO photoanodes under visibl light irradiation ($\lambda > 420$ nm) at a applied potential of 1.5 V. (d) HPLC graphs of PEC degradation of phenol at different reaction times by using 15% g-C_3N_4@ZnO photoanode. (e) PC degradation rate of phenol using g-C_3N_4 and g-C_3N_4@ZnO photoanodes under UV light irradiation ($\lambda = 365$ nm). (f) PEC degradation rate of phenol over g-C_3N_4 and g-C_3N_4@ZnO photoanodes under UV light irradiation ($\lambda = 365$ nm) at an applied potential of 1.5 V.

the interface between ZnO core and g-C_3N_4 shell would be weakened with superfluous amount of g-C_3N_4, which may damage the interface and thus increased the possibility of combination of e^-/h^+ pairs. Compared with PC degradation, EC process of g-C_3N_4@ZnO composites (Fig. 6b) result in the relatively decreasing degradation rate, suggesting that visible light irradiation is principal for efficient degradation of phenol, and the rate constant k of 15% g-C_3N_4@ZnO is 0.173 h^{-1}, which was higher than other as-synthesized samples.

As shown in Fig. 6c, PEC process establishes a clear lead over the other processes in degradation of phenol, indicating that the applied bias potential greatly boosted the separation of the photogenerated electron-hole pairs effectively and prolonged the lifetime of the photogenerated charge carriers [68,69]. All g-C_3N_4@ZnO photoanodes show higher PEC activity under visible light irradiation compared with g-C_3N_4 photoanode. The PEC degradation rate constant of g-C_3N_4 and g-C_3N_4@ZnO photoanodes can be ranked the following order: 15% g-C_3N_4@ZnO > 20% g-C_3N_4@ZnO > 10% g-C_3N_4@ZnO > 5% g-C_3N_4@ZnO > 1% g-C_3N_4@ZnO > g-C_3N_4. Among all samples, 15% g-C_3N_4@ZnO photoanode exhibits the highest visible-light PEC activity and the rate constant of degradation phenol is determined to be 1.216 h^{-1}, which is about 3 times faster than that of PC degradation. After carefully analyzing k values of EC (0.173 h^{-1}), PC (0.396 h^{-1}) and PEC(1.216 h^{-1}) for 15% g-C_3N_4@ZnO, the con-

Table 1
PC, EC and PEC degradation phenol performance of $g\text{-}C_3N_4$ and $g\text{-}C_3N_4$@ZnO photoanodes under visible light irradiation.

Entry	Sample	Surface area	Pore volume	shell thickness	Pseudo-first order kinetic (k_{app}) h^{-1}		
	m^2/g	cm^3/g	(nm)	EC (Phenol)	PC(Phenol)	PEC (Phenol)	
1	$g\text{-}C_3N_4$	13.6 [70]	0.064 [70]	0	0.108	0.079	0.138
2	1%$g\text{-}C_3N_4$@ZnO	14.3	0.034	0	0.111	0.103	0.187
3	5%$g\text{-}C_3N_4$@ZnO	15.4	0.044	0	0.118	0.122	0.24
4	10%$g\text{-}C_3N_4$@ZnO	20	0.054	0	0.140	0.156	0.414
5	15%$g\text{-}C_3N_4$@ZnO	22.9	0.063	1.89	0.173	0.396	1.216
6	20%$g\text{-}C_3N_4$@ZnO	24.2	0.078	3.21	0.160	0.215	0.579

clusion has been obtained that k values of PEC process is higher than the combination EC and PC process, suggesting that the combination of photocatalysis and electrochemical do have an apparent synergistic effect, which is called "electrically assisted photocatalysis" [70]. Base on the above analysis, the enhanced PEC performance of 15% $g\text{-}C_3N_4$@ZnO photoanode can be attributed the aspects as follows: (1) The $g\text{-}C_3N_4$ shell in the $g\text{-}C_3N_4$@ZnO composites can promote wider spectral response, thereby inducing more photons to participate for the PEC degradation of phenol solution; (2) The appropriate thickness of $g\text{-}C_3N_4$ shell in the $g\text{-}C_3N_4$@ZnO composites exists a significant synergistic effect, which greatly enhance charge transfer and separation of photoinduced electro-hole pairs; (3) The applied bias provides a driving force to the separation of the photogenerated electron-hole pairs effectively and inhibits the recombination of holes and electrons. The degradation rate of phenol solution under different process (PC, EC and PEC) over $g\text{-}C_3N_4$ and $g\text{-}C_3N_4$@ZnO composites under visible light irradiation are summarized in Table 1.

In order to investigate PEC degradation of phenol and its degradation intermediates using 15% $g\text{-}C_3N_4$@ZnO composites as photoanode with visible light irradiation, HPLC chromatograms along with different irradiation time was utilized. It can be seen from Fig. 6d that except for the original phenol main peak at 3.61 min, only two small peaks were observed about 1.71 min. It was corresponding to benzoquinone (BQ), which is attributed to the self-degradation of initial phenol solution. Under visible light irradiation, the new peak of the lower fatty acid at 1.11 min appears after 1.5 h and the peak of catechol at 2.69 min appears after 0.5 h, suggesting the formation of intermediate products during the phenol PEC degradation process. As PEC degradation of phenol proceeds, the characteristic peak intensity of phenol at 3.61 min decreased gradually with the irradiation time extending, whereas the peaks of intermediate products (lower fatty acid, BQ) increased gradually. Furthermore, the peak intensity of catechol firstly increased to maximum value and then decreased after 1.5 h of PEC degradation, indicating that ring cleavage reaction has happened. Moreover, BQ can totally degraded without generating any further toxic products and only a small amount of catechol has been detected as conversion intermediate during the phenol PEC degradation process, suggesting that 15% $g\text{-}C_3N_4$@ZnO photoanode can degrade phenol rapidly to form small molecular organic acids, which was mineralized into CO_2 and H_2O. Fig.S5 exhibits the removal percentage of phenol and the extent of mineralization of 15% $g\text{-}C_3N_4$@ZnO photoanode at the different reaction time during PEC degradation process. It can be seen from Fig.S5 that the TOC removal continuously increased at a lower rate comparing with the degradation efficiency of phenol and the degradation efficiency of phenol over 15% $g\text{-}C_3N_4$@ZnO photoanode has reached 97.3% after 3 h, whereas the TOC removal percentage of phenol was 69.7%. The results have been proved by the HPLC chromatogram. Some intermediates like small molecular organic acids were formed in the degradation of phenol, and intermediates would take a long time illumination for its total mineralization.

Although, the formation of core-shell structure $g\text{-}C_3N_4$@ZnO composites enhanced PC and PEC degradation of phenol under visible light irradiation, the UV activity of PC and PEC became progressively worse. It can be seen from Fig. 6e and f, the PC and PEC activity of the $g\text{-}C_3N_4$@ZnO photoanodes were much lower than the pure ZnO under UV light irradiation. Moreover, with an increasing of loading amount of $g\text{-}C_3N_4$, the PC and PEC activity were deteriorated gradually. As the loading amount of $g\text{-}C_3N_4$ was 15%, the apparent rate constant is 0.107 h^{-1} and 0.508 h^{-1} in the PC and PEC process, whereas the k of the pristine ZnO was 0.433 h^{-1} and 1.275 h^{-1}, respectively, suggesting that the $g\text{-}C_3N_4$ shell prevent UV light irradiation of ZnO, which lead to restraining the PC and PEC activity.

3.3. Proposed mechanism of enhanced visible-light PEC performance

It is well known that the photocatalytic activity is mainly determined by phase structure, surface area, and separation efficiency of photogenerated electrons and holes [72]. XRD shows that ZnO patticles haven't been changed the phase structure after the formation core-shell structure $g\text{-}C_3N_4$@ZnO composites, indicating that the modification of $g\text{-}C_3N_4$ did not influence the lattice structure of ZnO. Furthermore, comparing to the origin ZnO particles, the BET surface of $g\text{-}C_3N_4$@ZnO composites do not significantly change with the increase loading amount of $g\text{-}C_3N_4$ (The BET surface area of ZnO and 20% $g\text{-}C_3N_4$@ZnO composites were 14.38 and 22.12 $m^2\,g^{-1}$, shown in Fig.S6). Since a little increase of BET surface area in $g\text{-}C_3N_4$@ZnO composites is not decisive factor for enhancement of PEC degradation phenol, it can be inferred that the major factor is an enhancement of the e^-–h^+ separation efficiency, which is boosted by the special core-shell structure and the applied bias.

To further elucidate the mechanism of the core-shell structure 15% $g\text{-}C_3N_4$@ZnO photoanode on the degradation of phenol under visible light irradiation during the PEC process, the active species trapping experiment was systematically investigated by using tBuOH, N_2 and formic acid, which are acted as effective $^{\bullet}OH$, $^{\bullet}O_2^-$, and holes scavengers, respectively [15]. As shown in Fig. 7, PEC activity of 15% $g\text{-}C_3N_4$@ZnO photoanode under visible light irradiation, causes a dramatic change by the addition of N_2 and formic acid, suggesting that $^{\bullet}O_2^-$ and holes are the two main oxidative species. Moreover, the reduction speed of PEC activity with addition of N_2 is faster than that with addition of formic acid, indicating that $^{\bullet}O_2^-$ is the more important oxidative species than holes during the PEC degradation process. However, the PEC activity has no conspicuous change with the addition of tBuOH, confirming that $^{\bullet}OH$ isn't a main oxidative species. This result was further confirmed by ESR spin-trap measurements which were performed for indentifying reactive radicals. As shown in Fig. 8a, DMPO-$^{\bullet}O_2^-$ has much stronger signals under visible light irradiation and no obvious ESR signals of $^{\bullet}O_2^-$ were observed in the dark. At the same time, the pattern of DMPO-$^{\bullet}O_2^-$ has existed some extra peaks, which was a signal response of DMPOX for DMPO directly oxidized by holes [73]. In Fig. 8b, no ESR signals of $^{\bullet}OH$ was detected in the dark or under

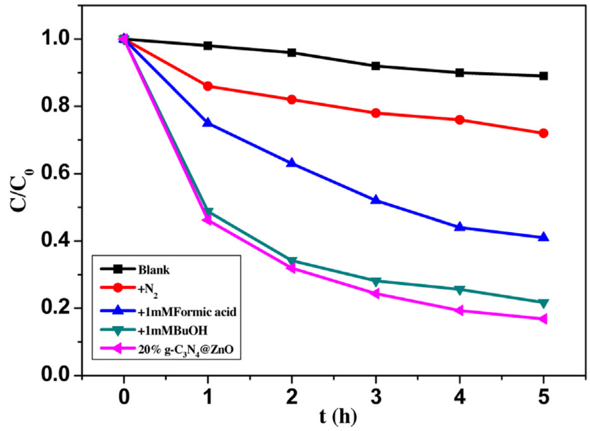

Fig. 7. The active species trapping by PEC degradation of phenol over 15% g-C_3N_4@ZnO photoanode under visible light irradiation with an applied bias 1.5 V.

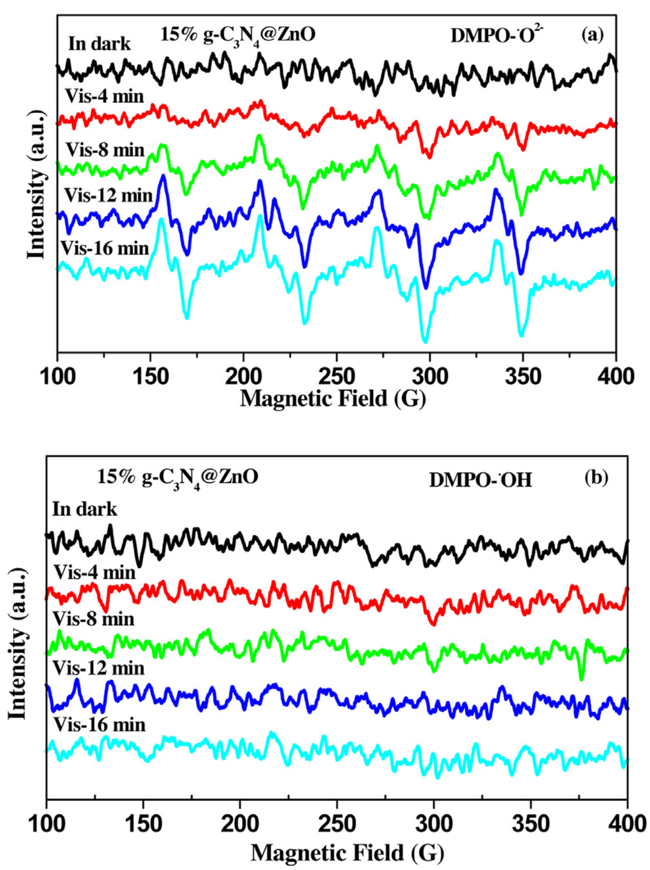

Fig. 8. DMPO spin-trapping ESR spectra of 15% g-C_3N_4@ZnO composites (a) DMPO-$\cdot O^{2-}$ in methanol dispersion; (b) DMPO-$\cdot$OH in water dispersion.

visible irradiation. These ESR results further demonstrate that $\bullet O_2^-$ is the dominant active specie in PEC degradation of phenol and holes also have affected this PEC progress.

The electrochemical impedance spectroscopy (EIS, presented as Nyquist plots) measurement was also used to investigate the interface separation and migration of the photoinduced charge carrier between ZnO core and g-C_3N_4 shell in the g-C_3N_4@ZnO composites. It is generally believed that the smaller arc radius on the EIS Nyquist plot represents a more effective interfacial charge transfer and faster separation of photo-generated electron-hole pairs [74]. Fig. 9 shows the EIS nyquist plots of g-C_3N_4 and g-C_3N_4@ZnO composites with visible light irradiation ($\lambda > 420$ nm) and the applied bias

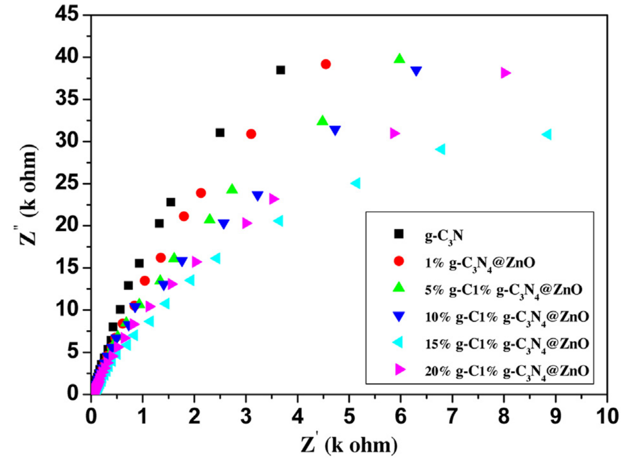

Fig. 9. Nyquist plots for g-C_3N_4 and g-C_3N_4@ZnO photoanodes in 0.1 M Na_2SO_4 aqueous solution under visible light irradiation.

voltage 1.5 V in the 0.1 M Na_2SO_4 eclectrolyte. It can be seen from Fig. 9 that the diameters of the arc radius for all of the g-C_3N_4@ZnO composites are smaller than g-C_3N_4 electrode. The diameters of the arc radius decreases gradually with an increasing of the loading amount of g-C_3N_4 and the diameter of the Nyquist semicircle for 15% g-C_3N_4@ZnO composites is the smallest, and then followed by an increasing trend with a further increase of g-C_3N_4 loading up to 20%, suggesting that 15% g-C_3N_4@ZnO composite has a suitable g-C_3N_4 shell thickness, which enhances the interface separation and immigration of photogenerated electron-hole pairs between g-C_3N_4 shell and ZnO core.

As presented above experimental results, a possible double synergistic mechanism for the PEC process which combined of special core-shell structures and electro-oxidation assisted photocatalysis, was proposed as illustrated in Fig. 10. When irradiated by visible light, g-C_3N_4 shell in the g-C_3N_4@ZnO composites can be excited and, then induce π-π^* transition which causes the transportation of excited-state electrons from the highest occupied molecular orbital (HOMO, 1.57 eV) to the lowest unoccupied molecular orbital (LUMO, −1.12 eV), while the holes remained in the HOMO of g-C_3N_4 which cannot generate $\bullet$OH by holes oxidizing OH^-/H_2O for the CB potential of g-C_3N_4 (1.40 eV) being lower than that of the potential of $OH^-/\bullet OH$ and $H_2O/\bullet OH$ (1.99 and 2.27 eV). At the same time, the LUMO of g-C_3N_4 is more negative than the CB edge of ZnO (-0.5 eV), the excited electrons on the LUMO of g-C_3N_4 across the interface can continuously transfer from the LUMO of g-C_3N_4 to CB of ZnO and along ZnO to the external circuit with an assistant of the applied bias, and finally transport to the ITO substrate and counter electrode. Thus, the efficient photoinduced charge separation accelerates the electron transfer process, which is faster than the recombination of photogenerated electron-hole pairs. The electrons of the ITO substrate and counter electrode which are more negative than $E(O_2/\bullet O^{2-})$ (−0.33 V vs. NHE), are a good reductant that could efficiently reduce oxygen molecules adsorbed on the surface of the photoanode to $\bullet O^{2-}$. Moreover, super-oxide radicals $\bullet O^{2-}$ are the most important oxidizing species and then induces the phenol degradation. Meanwhile, photo-generated holes which can accumulate in the HOMO of g-C_3N_4, have a powerful potential to capture electrons from adsorbed phenol molecules and oxidize phenol directly.

Namely, the enhancement of PEC activity of core-shell structure g-C_3N_4@ZnO photoanodes could be ascribed to the typical double synergistic mechanism. First, the synergistic interfacial interaction between ZnO core and g-C_3N_4 shell with matchable overlapping energy bands can force the photogenerated electrons in g-C_3N_4

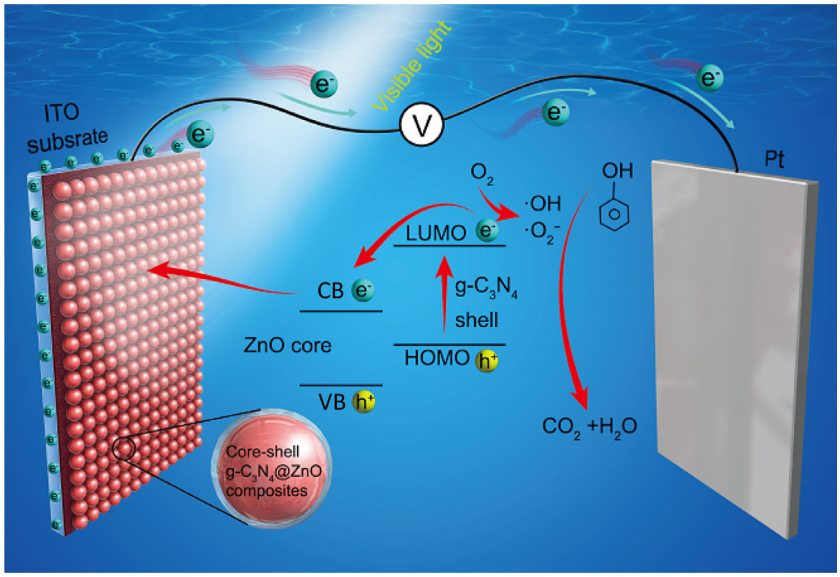

Fig. 10. Schematic diagram of PEC degradation of phenol using 15% g-C_3N_4@ZnO composites as photoanode and Pt as the counter electrode under visible light irradiation.

shell far away from the interfaces of g-C_3N_4@ZnO composites to facilitate the interface separation and immigration of photogenerated electron-hole pairs. Second, an applied potential has resulted in an obvious synergetic effect between the electrochemical and photocatalytic processes. The photogenerated electrons were taken away by an applied positive bias potential and eventually reach the ITO substrate and counter electrode through the external circuit. In such a way, the lifetime of the charge carriers was increased and the recombination of photogenerated electron-hole pairs was effectively inhibited, thus resulting in a high PEC degradation efficiency. Furthermore, water could evolve O_2 with an anodic bias of 1.5 V vs. SCE in the PEC process and then generate more active species $^\bullet O^{2-}$ which promoted to produce $^\bullet$OH by the $^\bullet O^{2-}$-H_2O_2-$^\cdot$OH route [75]. Therefore, various active species such $^\bullet O^{2-}$, holes and $^\bullet$OH involved in the PEC degradation of phenol and improved the efficiency of mineralization of the phenol. To evaluate the stability and reusability of 15% g-C_3N_4@ZnO composites, the circulating runs in the photocatalytic degradation of phenol under visible light irradiation was also investigated, and the results are shown in Fig.S7. It can seen that no conspicuous change of photocatalytic activity was observed after visible light irradiation for 5 circles, suggesting that the g-C_3N_4 shell in the g-C_3N_4@ZnO composites could inhibit the photocorrosion of ZnO and greatly enhance the stability of g-C_3N_4@ZnO composites.

4. Conclusion

In this work, a series of core-shell g-C_3N_4@ZnO composites using industrial grade ZnO nanoparticles as the starting materials meeting the requirements for practical applications, were successfully synthesized via an economical and facile reflux method at a low temperature 65 °C. Based on the electrochemical investigations, the core-shell g-C_3N_4@ZnO composites harvest visible-light absorption, promote the separation and transfer efficiency of photogenerated electron-hole pairs. Due to these unique core-shell structures, and the as-obtained g-C_3N_4@ZnO photoanodes show remarkably improved PEC performance comparing to PC and EC process under visible light irradiation. Among the prepared photoanodes, core-shell 15% g-C_3N_4@ZnO photoanode shows the best PEC performance and the rate constant value was 8.8 time as large as that of g-C_3N_4 photoanode for degradation of phenol with an anodic bias of 1.5 V vs. SCE, suggesting the double synergistic effects of core-shell structure and electro-oxidation assisted photocatalysis together in enhancing PEC performance.

Acknowledgements

The authors gratefully acknowledge the financial support of Natural Science Foundation of Liaoning (Grant NO. 2015020577), Foundation of Anshan Municipal Division of Science & Technology (Grant NO. 20140556), Talents Foundation of University of Science and Technology Liaoning (Grant NO. 2015RC10), the Scientific Research Foundation of the Educational Department of Liaoning Province (Grant NO. L2013122), Chinese National Science Foundation (Grant NO. 201437003, 21621003), National Basic Research Program of China (Grant NO. 2013CB632403) and Collaborative Innovation Center for Regional Environmental Quality.

Appendix A. Supplementary data

Supplementary data associated with this article can be found, in the online version, at http://dx.doi.org/10.1016/j.apcatb.2017.05.034.

References

[1] M.R. Hoffmann, S.T. Martin, C. Wongyong, D.W. Bahnemannt, Environmental applications of semiconductor photocatalysis, Chem. Rev. 95 (1995) 69–96.
[2] L. Yu, J. Liu, X. Xu, L. Zhang, R. Hu, J. Liu, L. Yang, M. Zhu, Metal-organic framework-derived NiSb alloy embedded in carbon hollow spheres as superior lithium-ion battery anodes, ACS Appl. Mater. Interfaces 9 (2017) 2516–2525.
[3] L. Wei, Y. Chen, Y. Lin, H. Wu, R. Yuan, Z. Li, MoS_2 as non-noble-metal co-catalyst for photocatalytic hydrogen evolution over hexagonal $ZnIn_2S_4$ under visible light irradiations, Appl. Catal. B: Environ. 144 (2014) 521–527.
[4] W.J. Sheng, B. Sun, T.L. Shi, X.H. Tan, Z.C. Peng, G.L. Liao, Quantum dot-sensitized hierarchical micro/nanowire architecture for photoelectrochemical water splitting, ACS Nano 8 (2014) 7163–7169.
[5] I.S. Cho, Z.B. Chen, A.J. Forman, D.R. Kim, P.M. Rao, T.F. Jaramillo, X.L. Zheng, Branched TiO_2 nanorods for photoelectrochemical hydrogen production, Nano Lett. 11 (2011) 4978–4984.
[6] Y.J. Lin, S. Zhou, S.W. Wang, D.W. Wang, Nanonet-based hematite heteronanostructures for efficient solar water splitting, J. Am. Chem. Soc. 133 (2011) 2398–2401.
[7] S.V. Kershaw, A.S. Susha, A.L. Rogach, Narrow bandgap colloidal metal chalcogenide quantum dots: synthetic methods, heterostructures, assemblies, electronic and infrared optical properties, Chem. Soc. Rev. 42 (2013) 3033–3087.

[8] H. Li, X. Wang, J.Q. Xu, Q. Zhang, Y. Bando, D. Gollberg, Y. Ma, T.Y. Zhai, One-dimensional CdS nanostructures: a promising candidate for optoelectronics, Adv. Mater. 25 (2013) 3017–3037.
[9] C.Y. Zhai, M.S. Zhu, F.Z. Pang, D. Bin, C. Lu, M.C. Goh, P. Yang, Y.K. Du, High efficiency photoelectrocatalytic methanol oxidation on CdS quantum dots sensitized Pt electrode, ACS Appl. Mater. Interfaces 8 (2016) 5972–5980.
[10] Z.X. Zhou, J.H. Wang, J.C. Yu, Y.F. Shen, Y. Li, A.R. Liiiu, S.Q. Lin, Dissolution and liquid crystals phase of 2D polymeric carbon nitride, J. Am. Chem. Soc. 137 (2015) 2179–2182.
[11] P. Niu, L.L. Zhang, G. Liu, H.M. Cheng, Graphene-like carbon nitride nanosheets for improved photocatalytic activities, Adv. Funct. Mater. 22 (2012) 4763–4770.
[12] X.D. Zhang, X. Xie, H. Wang, J.J. Zhang, B.C. Pan, Y. Xie, Enhanced photoresponsive ultrathin graphitic-phase C_3N_4 nanosheets for bioimaging, J. Am. Chem. Soc. 135 (2013) 18–21.
[13] L. Ci, L. Song, C.H. Jin, D. Jariwala, D.X. Wu, Y.J. Li, A. Srivastava, Z.F. Wang, K. Storr, L. Balicas, F. Liu, P.M. Ajayan, Atomic layers of hybridized boron nitride and graphene domains, Nat. Mater. 9 (2010) 430–435.
[14] D.M. Chem, K.W. Wang, T.Z. Ren, H. Ding, Y.F. Zhu, Synthesis and characterization of the ZnO/mpg-C_3N_4 heterojunction photocatalyst with enhanced visible light photoactivity, Dalton Trans. 43 (2014) 13105–13114.
[15] Y.J. Wang, R. Shi, J. Lin, Y.F. Zhu, Enhancement of photocurrent and photocatalytic activity of ZnO hybridized with graphite-like C_3N_4, Energy Environ. Sci. 4 (2011) 2922–2929.
[16] J.W. Zhou, M. Zhang, Y.F. Zhu, Preparation of visible light-driven g-C_3N_4@ZnO hybrid photocatalyst via mechanochemistry, Phys. Chem. Chem. Phys. 16 (2014) 17627–17633.
[17] D.M. Chen, K.W. Wang, D.G. Xiang, R.L. Zong, W.Q. Yao, Y.F. Zhu, Significantly enhancement of photocatalytic performances via core-shell structure of ZnO@ mpg-C_3N_4, Appl. Catal., B 147 (2014) 554–561.
[18] J. Xiao, X. Zhang, Y. Li, A ternary g-C_3N_4/Pt/ZnO photoanode for efficient photoelectrochemical water splitting, Int. J. Hydrogen Energy 40 (2015) 9080–9087.
[19] S.P. Adhikari, H.R. Pant, H.J. Kim, C.H. Park, C.S. Kam, Deposition of ZnO flowers on the surface of g-C_3N_4 sheets via hydrothermal process, Ceram. Int. 41 (2015) 12923–12929.
[20] J. Georgieva, S. Armyanov, E. Valova, I. Poulios, S. Sotiropoulos, Enhanced photocatalytic activity of electrosynthesised tungsten trioxide-titanium dioxide bi-layer coatings under ultraviolet and visible light illumination, Electrochem. Commun. 7 (2007) 365–370.
[21] S. Kumar, A. Baruah, S. Tonda, B. Kumar, V. Shanker, B. Sreedhar, Cost-effective and eco-friendly synthesis of novel and stable N-doped ZnO/g-C_3N_4 core-shell nanoplates with excellent visible-light responsive photocatalysis, Nanoscale 6 (2014) 4830–4842.
[22] H. Qin, W. Li, Y. Xia, T. He, Photocatalytic activity of heterostructures based on ZnO and N-doped ZnO, ACS Appl. Mater. Interfaces 3 (2011) 3152–3156.
[23] S. Rehman, R. Ullah, A.M. Butt, N.D. Gohar, Strategies of making TiO_2 and ZnO visible light active, J. Hazard. Mater. 170 (2009) 560–569.
[24] K. Maeda, T. Takata, M. Hara, N. Saito, Y. Inoue, H. Kobayashi, K. Domen, GaN: ZnO solid solution as a photocatalyst for visible-light-driven overall water splitting, J. Am. Chem. Soc. 127 (2005) 8286–8287.
[25] S.P. Adhikari, H.R. Pant, J.H. Kim, H.J. Kim, C.H. Park, C.S. Kim, One pot synthesis and characterization of Ag-ZnO/g-C_3N_4 photocatalyst with improved photoactivity and antibacterial properties: colloids and Surfaces A: physicochem, Eng. Aspects 482 (2015) 477–484.
[26] L.Q. Jing, B.Q. Wang, B.F. Xin, S.D. Li, K.Y. Shi, W.M. Cai, H.G. FU, Investigations on the surface modification of ZnO nanoparticle photocatalyst by depositing Pd, J. Solid State Chem. 177 (2004) 4221–4227.
[27] A. Stroyuk, V.V. Shvalagin, S.Y. Kuchmii, Photochemical synthesis, spectral-optical and electrophysical properties of composite nanoparticles of ZnO/Ag, Theor. Exp. Chem. 40 (2004) 98–104.
[28] M.L. Zhang, T.C. An, X.H. Hu, C. Wang, G.Y. Sheng, J.M. Fu, Preparation and photocatalytic properties of a nanometer ZnO-SnO_2 coupled oxide, Appl. Catal., A 260 (2004) 215–222.
[29] X.X. Gao, J. Wang, J.L. Yu, H.B. Xu, Novel ZnO-ZnS nanowire arrays with heterostructures and enhanced photocatalytic properties, CrystEngComm 17 (2015) 6328–6337.
[30] G. Yu, J. Gao, J.C. Hummelen, F. Wudl, A.J. Heeger, Polymer photovoltaic cells: enhanced efficiencies via a network of internal donor-Acceptor heteroiunctions, Science 270 (1995) 1789–1791.
[31] R. Comparelli, E. Fanizza, M.L. Curri, P.D. Cozzoli, G. Mascolo, A. Agostiano, UV-induced photocatalytic degradation of azo dyes by organic-capped ZnO nanocrystals immobilized onto substrates, Appl. Catal., A 60 (2005) 1–11.
[32] W. Jo, N.C.S. Selvam, Enhanced visible light-driven photocatalytic performance of ZnO-g-C_3N_4 coupled with graphene oxide as a novel ternary nanocomposite, J. Hazard. Mater. 299 (2015) 462–470.
[33] W. Jo, J.Y. Lee, N.C.S. Selvam, Synthesis of MoS_2 nanosheets loaded ZnO-g-C_3N_4 nanocomposites for enhanced photocatalytic applications, Chem. Eng. J. 289 (2016) 306–318.
[34] F. Goettmann, A. Fischer, M. Antonietti, A. Thomas, Chemical synthesis of mesoporous carbon nitrides using hard templates and their use as a metal-Free catalyst for friedel-Crafts reaction of benzene, Angrew. Chem. 45 (2006) 4467–4471.
[35] H. Fu, T. Xu, S. Zhu, Photocorrosion inhibition and enhancement of photocatalytic activity for ZnO via hybridization with C_{60}, Environ. Sci. Tecchnol. 42 (2008) 8064–8069.
[36] H. Zhang, Y. Zhu, Significant visible photoactivity and antiphotocorrosion performance of CdS photocatalysts after monolayer polyaniline hybridization, J. Phys. Chem. C 114 (2010) 5822–5826.
[37] X.H. Li, J.S. Chen, X. Wang, J. Sun, M. Antonietti, Metal-free activation of dioxygen by graphene/g-C_3N_4 nanocomposites: functional dyads for selective oxidation of saturated hydrocarbons, J. Am. Chem. Soc. 133 (2011) 8074–8077.
[38] Q. Xiang, J. Yu, M. Jaroniec, Preparation and enhanced visible-light photocatalytic H2-production activity of graphene/C_3N_4 composites, J. Phys. Chem. C 115 (2011) 7355–7363.
[39] J. Xu, Y. Wang, Y. Zhu, Nanoporous graphitic carbon nitride with enhanced photocatalytic performance, Langmuir 29 (2013) 10566–10572.
[40] S. Liu, F. Chen, S. Li, X. Peng, Y. Xiong, Monodisperse bismuth nanoparticles decorated graphitic carbon nitride: enhanced visible-Light-Response photocatalytic NO removal and reaction pathway, Appl. Catal. B 205 (2017) 532–540.
[41] M. Zhang, J. Xu, R. Zong, Y. Zhu, Enhancement of visible light photocatalytic activities via porous structure of g-C_3N_4, Appl. Catal. B 147 (2014) 229–235.
[42] X. Wang, X. Chen, A. Thomas, X. Fu, M. Antonietti, Metal-containing carbon nitride compounds: a new functional organic-Metal hybrid material, Adv. Mater. 21 (2009) 1609–1612.
[43] F. Dong, Z. Zhao, Y. Sun, Y. Sun, Y. Zhang, S. Yan, Z. Wu, An advanced semimetal-organic bi spheres-g-C_3N_4 nanohybrid with SPR-enhanced visible-light photocatalytic performance for NO purification, Environ. Sci. Technol. 49 (20) (2015) 12432–12440.
[44] G. Liu, P. Niu, C. Sun, S.C. Smith, Z. Chem, G.Q. Lu, H.M. Cheng, Unique electronic structure induced high photoreactivity of sulfur-doped graphitic C_3N_4, J. Am. Chem. Soc. 132 (2010) 11642–11648.
[45] J.S. Zhang, M.W. Wang, C. Yang, X.C. Wang, Helical graphitic carbon nitrides with photocatalytic and optical activities, Angew. Chem. Int. Ed. 53 (2014) 11926–11930.
[46] G.G. Zhang, M.W. Zhang, X.X. Ye, X.Q. Qiu, S. Lin, X.C. Wang, Iodine modified carbon nitride semiconductors as visible light photocatalysts for hydrogen evolution, Adv. Mater. 26 (2014) 805–809.
[47] Y.J. Cui, Z.X. Ding, X.Z. Fu, X.C. Wang, Construction of conjugated carbon nitride nanoarchitectures in solution at low temperatures for photoredox catalysis, Angew. Chem. Int. Ed. 51 (2012) 10145–10149.
[48] X.J. Bai, L. Wang, R.L. Zong, Y.F. Zhu, Photocatalytic activity enhanced via g-C_3N_4 nanoplates to nanorods, J. Phys. Chem. C 117 (2013) 9952–9961.
[49] Q.J. Xiang, J.G. Yu, M. Jaroniec, Preparation and enhanced visible-light photocatalytic H2-production activity of graphene/C_3N_4 composites, J. Phys. Chem. C 115 (2011) 7355–7363.
[50] Y. Zhang, Z. Chen, S. Liu, Y. Xu, Size effect induced activity enhancement and anti-photocorrosion of reduced graphene oxide/ZnO composites for degradation of organic dyes and reduction of Cr (VI) in water, Appl. Catal., B 140–141 (2013) 598–607.
[51] R. Zou, G. He, K. Xu, Q. Liu, Z. Zhang, J. Hu, ZnO nanorods on reduced graphene sheets with excellent field emission, gas sensor and photocatalytic properties, J. Mater. Chem. A 1 (2013) 8445–8452.
[52] Y.J. Wang, Z.X. Wang, S. Muhammad, H. He, Graphite-like C_3N_4 hybridized $ZnWO_4$ nanorods: synthesis and its enhanced photocatalysis in visible light, CryEngComm 14 (2012) 5065–5070.
[53] K. Santosh, T. Surendar, B. Arabinda, S. Vishnu, Synthesis of a novel and stable g-C_3N_4-Ag_3PO_4 hybrid nanocomposite photocatalyst and study of the photocatalytic activity under visible light irradiation, J. Mater. Chem. A 1 (2013) 5333–5340.
[54] X.J. Wang, W.Y. Yang, F.T. Li, Y.B. Xue, R.H. Liu, Y.J. Hao, In situ microwave-assisted synthesis of porous N-TiO_2/g-C_3N_4 heterojunctions with enhanced visible-light photocatalytic properties, Ind. Eng. Chem. Res. 52 (2013) 17140–17150.
[55] C. Pan, J. Xu, Y. Wang, D. Li, Y. Zhu, Dramatic activity of C_3N_4/$BiPO_4$ photocatalyst with core/shell structure formed by self-assembly, Adv. Funct. Mater. 22 (2012) 1518–1524.
[56] Y.J. Wang, X.J. Bai, C.S. Pan, J. He, Y.F. Zhu, Enhancement of photocatalytic activity of Bi_2WO_6 hybridized with graphite-like C_3N_4, J. Mater. Chem. 22 (2012) 11568–11573.
[57] R.C. Pawar, Y. Son, J. Kim, S.H. Ahn, C.S. Lee, Integration of ZnO with g-C_3N_4 structures in core-shell approach via sintering process for rapid detoxification of water under visible irradiation, Curr. Appl. Phys. 16 (2016) 101–108.
[58] F.F. Liang, Y.F. Zhu, Enhancement of mineralization ability for phenol via synergetic effect of photoelectrocatalysis of g-C_3N_4 film, Appl. Catal. B 180 (2016) 324–329.
[59] M. Zhang, J. Xu, R.L. Zong, Y.F. Zhu, Enhancement of visible light photocatalytic activities via porous structure of g-C_3N_4, Appl. Catal. B 147 (2014) 229–235.
[60] F. Cheng, H. Wang, X. Dong, The amphoteric properties of g-C_3N_4 nanosheets and fabrication of their relevant heterostructure photocatalysts by an electrostatic re-assembly route, Chem. Commun. 51 (2015) 7176–7179.
[61] X. Zhao, Y.F. Zhu, Synergetic degradation of rhodamine B at a porous $ZnWO_4$ film electrode by combined electro-oxidation and photocatalysis, Environ. Sci. Technol. 40 (2006) 3367–3372.
[62] X.J. Bai, S.C. Yan, J.J. Wang, L. Wang, W.J. Jiang, Y.F. Zhu, A simple and efficient strategy for the synthesis of a chemically tailored g-C_3N_4 material, J. Mater. Chem. A 2 (2014) 17251–17259.
[63] Y.C. Zhao, D.L. Yu, H.W. Zhou, Y.J. Tian, O. Yangagisawa, Turbostratic carbon nitride prepared by pyrolysis of melamine, J. Mater. Sci. 40 (2005) 2645–2647.

[64] X. Li, J. Zhang, L. Shen, Y. Ma, W. Lei, Q. Cui, G. Zou, Preparation and characterization of graphitic carbon nitride through pyrolysis of melamine, Appl. Phys. A 94 (2009) 387–392.
[65] D. Wu, K. Cao, F. Wang, H. Wang, Z. Gao, F. Xu, Y. Guo, K. Jiang, Two dimensional graphitic-phase C_3N_4 as multifunctional protecting layer for enhanced short-circuit photocurrent in ZnO based dye-sensitized solar cells, Chem. Eng. J. 280 (2015) 441–447.
[66] D. Liu, W.Q. Yao, J. Wang, Y.F. Liu, M. Zhang, Y.F. Zhu, Enhanced visible light photocatalytic performance of a novel heterostructured $Bi_4O_5Br_2/Bi_{24}O_{31}Br_{10}/Bi_2SiO_5$ photocatalyst, Appl. Catal., B 172–173 (2015) 100–107.
[67] P. Kuang, J. Ran, Z. Liu, H. Wang, N. Li, Y. Su, Y. Jin, S. Qiao, Enhanced photoelectrocatalytic activity of BiOI nanoplate-zinc oxide nanorod p-n heterojunction, Chem. Eur. J. 21 (2015) 15360–15368.
[68] G. Li, L. Wu, F. Li, P. Xu, D. Zhang, H. Li, Photoelectrocatalytic degradation of organic pollutants via a CdS quantum dots enhanced TiO_2 nanotube array electrode under visible light irradiation, Nanoscale 5 (2013) 2118–2125.
[69] Z. Hua, Z. Dai, X. Bai, Z. Ye, P. Wang, H. Gu, X. Hua, Copper nanoparticles sensitized TiO_2 nanotube arrays electrode with enhanced photoelectrocatalytic activity for diclofenac degradation, Chem. Eng. J. 283 (2016) 514–523.
[70] Y. Zhang, Y. Jin, X. Huang, H. Shi, G. Zhao, H. Zhao, Nanocrystalline {001} TiO_2/carbon aerogel electrode with high surface area and enhanced photoelectrocatalytic oxidation capacity, Electrochim. Acta 130 (2014) 194–199.
[72] J.C. Yu, J. Yu, W. Ho, L. Zhang, Preparation of highly photocatalytic active nano-sized TiO_2 particles via ultrasonic irradiation, Chem. Commun. 19 (2001) 1942–1943.
[73] T. Xiong, F. Dong, Y. Zhou, M. Fu, W.K. Ho, New insights into how RGO influences the photocatalytic performance of $BiOIO_3$/RGO nanocomposites under visible and UV irradiation, J. Colloid Interface Sci. 447 (2015) 16–24.
[74] W.H. Leng, Z. Zhang, J.Q. Zhang, C.N. Cao, Investigation of the kinetics of a TiO_2 photoelectrocatalytic reaction involving charge transfer and recombination through surface states by electrochemical impedance spectroscopy, J. Phys. Chem. B 109 (2005) 15008–15023.
[75] Z. Ni, F. Dong, H. Huang, Y. Zhang, New insights into how Pd nanoparticles influence the photocatalytic oxidation and reduction ability of g-C_3N_4 nanosheets, Catal. Sci. Technol. 6 (2016) 6448–6458.

Further reading

[71] J. Xu, Y.J. Wang, Y.F. Zhu, Nanoporous graphitic carbon nitride with enhanced photocatalytic performance, Langmuir 29 (2013) 10566–10572.